Masanori Saito[1,*] and Ping Yang[1]

[1]Department of Atmospheric Sciences, Texas A&M University, College Station, TX, USA.

Corresponding author: Masanori Saito (masa.saito@tamu.edu)

Key Points:

- Bulk dust backscattering property models for lidar wavelengths are developed.
- The lidar ratio is more sensitive to particle shape than to particle size.
- Computed spectral backscattering properties are reasonably consistent with lidar observations of dust plumes.

Abstract

Sensitivities of the backscattering properties to microphysical properties (in particular, size and shape) of mineral dust aerosols are examined based on TAMUdust2020, a comprehensive single-scattering property database of irregular aerosol particles. We develop the bulk mineral dust particle models based on size-resolved particle ensembles with randomly distorted shapes and spectrally resolved complex refractive indices, which are constrained with in-situ observations reported in the literature. The lidar ratio is more sensitive to particle shape than particle size, while the depolarization ratio is sensitive to particle size. The simulated bulk backscattering properties (i.e., the lidar ratio and the depolarization ratio) of typical mineral dust particles with effective radii of 0.5–3 µm are reasonably consistent with lidar observations made during several field campaigns. The dust bulk optical property models are applicable to lidar-based remote sensing of dust aerosol properties.

Plain Language Summary

Lidar (Light Detection and Ranging) measurements help investigate atmospheric mineral dust aerosol properties. However, it has long been a challenge to interpret lidar signals, namely the backscattering properties, towards inferring mineral dust particle properties. This study is aimed to develop appropriate bulk mineral dust optical property models for simulating the backscattering properties. The present simulations demonstrate the significant impacts of mineral dust particle shape and size on backscattering by these particles. The developed mineral dust particle models will benefit lidar-based remote sensing of mineral dust plumes.

1 Introduction

Dust aerosol plumes have received significant attention over several decades due to their complex role in Earth's atmosphere energy system. Atmospheric mineral dust particles modulate the direct radiative effect (DRE) through scattering and absorption of atmospheric radiation (Kok et al., 2017) and their influence on cloud microphysical processes, namely, aerosol-cloud interactions (DeMott et al.,

2003; Bangert et al., 2012). These particles exhibit various sizes, shapes, and mineralogical compositions (Reid et al., 2003a; Kandler et al., 2009), leading to substantial regional variations of dust aerosol optical properties (Sokolik & Toon, 1999; Di Biagio et al., 2019). Due to dust emission events in small source regions (Haywood et al., 2003) and intercontinental transport of dust plumes (Prospero & Carlson, 1972; Duce et al., 1980), the impact of mineral dust aerosols spans from regional to global scales. As a result, current estimates of the dust DRE have significant uncertainties and potentially regional biases (Di Biagio et al., 2020).

Ground-based, airborne, and spaceborne observations of mineral dust plumes are essential to constrain the regional and global dust DRE. In contrast to passive sensor instruments, a lidar system can vertically resolve aerosol properties. Historically, aerosol extinction profiles are converted from lidar measurements by solving the lidar equation (Fernald et al., 1984; Klett, 1985), which requires an empirically predetermined lidar ratio. To date, state-of-the-science lidar systems incorporate capabilities of multiple channels, high-spectral resolution, and polarization, thereby providing vertical profiles of the spectral extinction coefficient, lidar ratio, and depolarization ratio of aerosol plumes (Groß et al., 2011; Haarig et al., 2018). These sophisticated lidar systems have been deployed in ground-based lidar networks (Sugimoto et al., 2008; Ansmann et al., 2003), aircraft-based field campaigns (Hair et al., 2008; Burton et al., 2015), and spaceborne payloads (Yorks et al., 2016; Illingworth et al., 2015).

However, the theoretical interpretation of lidar backscattering properties of dust plumes has long been a significant challenge due to computational difficulties associated with particle nonsphericity and large sizes of mineral dust particles. As the Lorenz–Mie theory applies only to spherical particles, the backscattering properties of nonspherical mineral dust particles are computed with other light-scattering computational methods (Mishchenko et al., 1997; Ishimoto et al., 2010; Kahnert et al., 2020). These methods are practically limited to particles with size parameters up to ~50 due to an enormous computational burden. The size parameter limit, corresponding to a particle diameter of ~2.82 µm at 355 nm, is much smaller than actual dust particles, many as large as 10–20 µm (Kandler et al., 2009) and some >75 µm (van der Does et al., 2018). The conventional geometric optics method applicable to the scattering property simulation of large nonspherical particles leads to substantial uncertainties in the backscattering simulations due to the inherent shortcomings of this method. Consequently, the understanding of the relationship between mineral dust aerosol particles' backscattering properties and microphysical properties remains inadequate.

Recently, light-scattering computational capabilities have been significantly enhanced toward more accurate modeling of the backscattering properties of nonspherical particles in the entire size range from the Rayleigh regime to the geometric optics regime (Yang et al. 2019), based on a combination of the invariant imbedding T-matrix method (Johnson, 1988; Bi et al. 2013) and the physical geometric optics method (Yang & Liou, 1996, 1997; Bi et al., 2011; Sun

et al. 2017). With these advanced light-scattering computational capabilities and a realistic nonspherical particle shape model, Saito et al. (2021) developed a comprehensive database of the single-scattering properties of irregular aerosol particles, TAMUdust2020, covering the entire practical range of particle sizes, wavelengths, and complex refractive indices (CRI) of mineral dust particles. Therefore, it is now feasible to develop a robust bulk optical property model of mineral dust aerosols for lidar applications. This study attempts to appropriately link the backscattering properties to the microphysical properties of mineral dust aerosols using the TAMUdust2020 database. Sections 2, 3, and 4 describe the bulk optical property model, discuss the results, and summarize the present findings, respectively.

2 Bulk dust aerosol optical property modeling

2.1 Assumptions and definitions of the particle size and shape

For robust simulations of the backscattering properties of mineral dust aerosols, it is essential to use realistic particle characteristics and minimize inappropriate assumptions. In this study, we postulate that 1) particles are randomly oriented, 2) particles have internally homogeneous compositions, and 3) an ensemble of 20 irregular hexahedral particles can approximate typical particle shapes of mineral dust aerosols. The first postulate is well justified because typical dust particles have small Reynolds numbers unless they undergo an extremely strong electric field (Ulanowski et al., 2007). The second postulate may be arguable, as mineral dust particles exhibit complex inner structures with multiple mineralogical compositions (Lindqvist et al., 2014). However, as such internal structural information is not generally available, this postulate is essential. The third postulate is partly verified through direct comparisons of the scattering properties of the assumed particle shape models and observed counterparts (Bi et al., 2010; Saito et al., 2021). However, the consistency of the geometric properties between the assumed particles and those of observed particles is not yet adequately verified.

The particle aspect ratio is one of the essential factors determining the single-scattering properties (Mishchenko et al., 1997; Huang et al., 2015) and the terminal velocity of particles (Ginoux, 2003). However, typical aspect ratios of mineral dust particles are uncertain because the definition of the aspect ratio varies in the literature. Therefore, it is necessary to relate the geometric properties of the assumed particle shape model to several particle aspect ratio definitions to utilize the previous findings reported in the literature.

The TAMUdust2020 database defines the maximum diameter (D) in terms of the smallest circumscribed sphere of a particle. In contrast, most previous studies employ the projected area-equivalent sphere diameter (D_{A}) to arrange size-dependent particle aspect ratios. Three "aspect ratio" definitions are used as, 1) the ratio of the maximum length to the perpendicular length of the two-dimensional (2D) projected shape ($\varepsilon_{\mathrm{proj}} = \frac{D_{\mathrm{proj}}}{W_{\mathrm{proj}}}$), 2) the ratio of the maximum length to the minor axis of an ellipsoid with the same projected area as the

particle ($\varepsilon_{\mathrm{el}} = \frac{\pi D_{\mathrm{proj}}^2}{4A_{\mathrm{proj}}}$), and 3) the ratio of the maximum length to its maximum perpendicular length (L_1) of a particle ($\varepsilon_{\mathrm{geo}} = \frac{D}{L_1}$). As these aspect ratios depend on particle orientations, we specify these aspect ratio definitions for randomly oriented particles by considering numerous orientations.

Figures 1 shows the geometric characteristics of 20 irregular hexahedral particles defined by Saito et al. (2021). Unlike a sphere or spheroidal particle model, the axis ratios of these particles are not unity (Figs. 1a–b). The aspect ratios of these particles range over $\varepsilon_{\mathrm{el}} \in [1.4,\ 2.4]$ and $\varepsilon_{\mathrm{proj}} \in [1.1,\ 1.9]$ (Fig. 1c). Okada et al. (2001) suggested that most mineral dust particles sampled in China have $\varepsilon_{\mathrm{proj}} < 2$. Also, Kandler et al. (2011) showed that typical particle aspect ratios defined by an ellipsoidal fit ($\varepsilon_{\mathrm{el}}$) fall within 1.3–2.5. Therefore, the geometric properties of the present irregular hexahedral particle models are fairly consistent with those of natural mineral dust particles, which confirms the validity of the third assumption in this study. In addition, the aspect ratio of individual convex particles can relate to the degree of sphericity (Ψ) (Fig. 1c), defined as (Wadell, 1935)

$$\Psi = \frac{\pi^{\frac{1}{3}}(6V)^{\frac{2}{3}}}{A_{\mathrm{s}}}, \quad (1)$$

where V and A_{s} are the particle volume and total surface area, respectively.

Figure 1d illustrates the mixing ratio (f_{mix}) of individual irregular hexahedral particles for an ensemble model defined by the ensemble-weighted degree of sphericity (Ψ_{ens}), described as

$$\Psi_{\mathrm{ens}} = \frac{\pi^{\frac{1}{3}}(6V_{\mathrm{ens}})^{\frac{2}{3}}}{A_{\mathrm{s,ens}}}, \quad (2)$$

where $V_{\mathrm{ens}} = \sum_{i=1}^{20} 6 f_{\mathrm{mix},i} V_i$, $A_{\mathrm{s,ens}} = \sum_{i=1}^{20} f_{\mathrm{mix},i} A_{\mathrm{s},i}$, and $\sum_{i=1}^{20} f_{\mathrm{mix},i} = 1$ (Saito et al. 2021). Based on these particle geometries and mixing ratios, the ensemble-weighted axis ratios and aspect ratios are computed for various irregular hexahedral ensemble models (Figs. 1e–f). Overall, the ensemble-weighted axis ratios and aspect ratios increase as Ψ_{ens} decreases. These monotonic relationships directly relate various literature-reported aspect ratios to Ψ_{ens} of the irregular hexahedral ensemble models (the ε–Ψ_{ens} relation). In addition, the $\frac{D}{D_{\mathrm{A}}}$ ratio varies with Ψ_{ens}, particularly when a 2D projected particle with a smaller Ψ_{ens} is more aspherical (Fig. 1e).

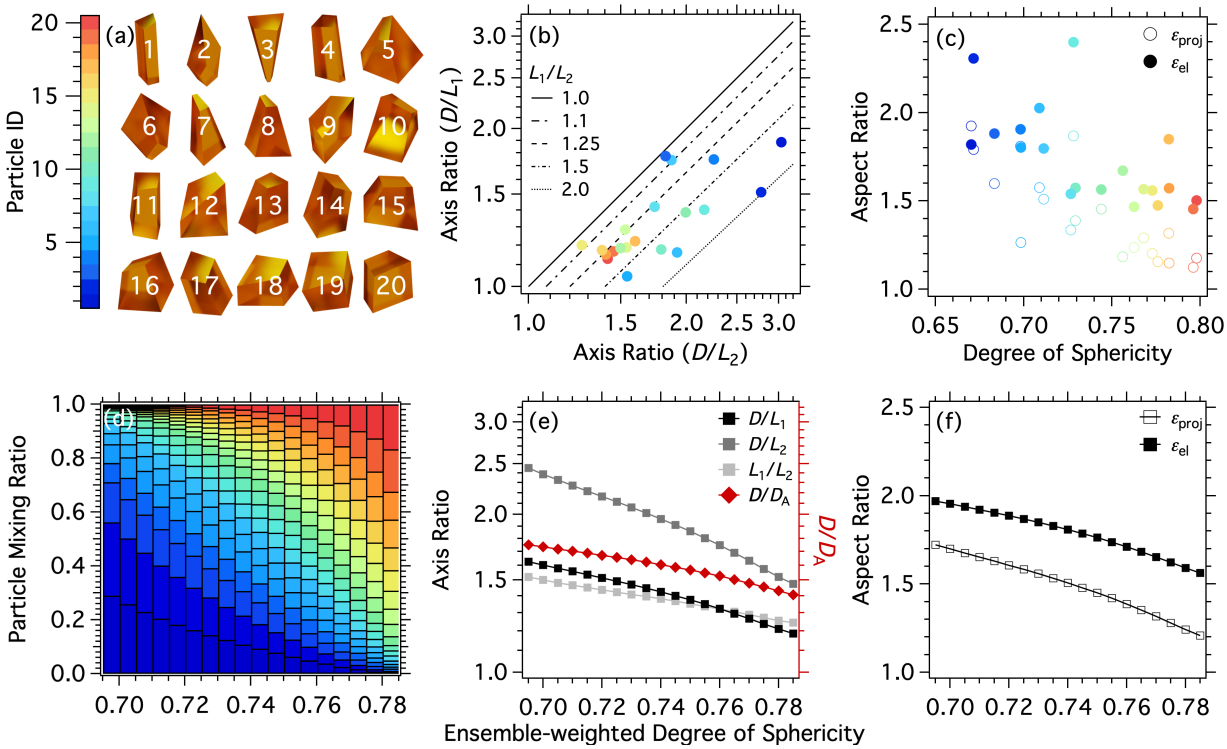

Figure 1. Geometric properties of 20 irregular hexahedral particles and those ensemble models, including (a) rendered graphics, (b) axis ratios, and (c) relation between the aspect ratio and the degree of sphericity of 20 irregular hexahedral particles in the upper panels, and (d) particle mixing ratios of individual particles for various ensemble models, (e) ensemble-weighted axis ratios and size ratio, and (f) aspect ratios of these ensemble models. Colors in panels (a–d) indicate individual irregular hexahedral particles.

2.2 Size-dependent particle shape ensemble model

To consider realistic geometric properties in this study, we review reported particle aspect ratios. Huang et al. (2020) compiled the median and geometric standard deviation of mineral dust particle aspect ratios reported in the literature, assuming a modified lognormal distribution of aspect ratios (Kandler et al., 2007). Among particle aspect ratio statistics available in Table S2 of Huang et al. (2020), we choose 18 natural airborne mineral dust cases that did not undergo any interaction with hydrometeors (e.g., ice nucleation or deposition onto snow), as summarized in Table 1.

Table 1. List of the publications that report in-situ measured particle shapes and complex refractive indices (CRIs) of mineral dust particles sampled across the globe. The "Bins" column lists the number of size bins used in the literature, and the size range of each bin is depicted in Fig. 2.

References	Abbr.	Particle size	Aspect ratio	CRI	Sample location	
		Bins	Def.			
Okada et al. (1987)	O87	1	D_{A}	$\varepsilon_{\mathrm{proj}}$	*N/A*	Nagoya, Japa
Okada et al. (2001)	O01Qir	1	D_{A}	$\varepsilon_{\mathrm{proj}}$	*N/A*	Qira, China
	O01Zha	1	D_{A}	$\varepsilon_{\mathrm{proj}}$	*N/A*	Zhangye, Chi
	O01Hoh	1	D_{A}	$\varepsilon_{\mathrm{proj}}$	*N/A*	Hohhot, Chir
Reid E. A. et al. (2003)	REA03	5	D_{A}	$\varepsilon_{\mathrm{el}}$	*N/A*	Puerto Rico
Reid J. S. et al. (2003)	RJS03	1	D_{A}	$\varepsilon_{\mathrm{el}}$	*N/A*	Puerto Rico
Kandler et al. (2007)	Ka07	6	D_{A}	$\varepsilon_{\mathrm{el}}$	*N/A*	Izana Tenerif
Chou et al. (2008)	Ch08	5	D_{A}	$\varepsilon_{\mathrm{el}}$	*N/A*	Niger
Coz et al. (2009)	Co09	2	D_{A}	$\varepsilon_{\mathrm{el}}$	*N/A*	Madrid, Spai
Kandler et al. (2009)	Ka09	1	D_{A}	$\varepsilon_{\mathrm{el}}$	2 cases	Tinfou, Moro
Kandler et al. (2011)	Ka11	2	D_{A}	$\varepsilon_{\mathrm{el}}$	*N/A*	Cape Verde
Scheuvens et al. (2011)	S11	4	D_{A}	$\varepsilon_{\mathrm{el}}$	*N/A*	Ourzazate, M
Lieke et al. (2011)	L11	5	D_{A}	$\varepsilon_{\mathrm{el}}$	*N/A*	Praia and Da
Klaver et al. (2011)	Kl11Nig	4	D_{A}	$\varepsilon_{\mathrm{el}}$	*N/A*	Niger
	Kl11Mal	4	D_{A}	$\varepsilon_{\mathrm{el}}$	*N/A*	Mali
Jeong et al. (2016)	J16	1	D	$\varepsilon_{\mathrm{geo}}$	*N/A*	Izana Tenerif
Rocha-Lima et al. (2018)	RL18Alg	1	D_{A}	$\varepsilon_{\mathrm{el}}$	*N/A*	Bordj Badji M
	RL18Mau	1	D_{A}	$\varepsilon_{\mathrm{el}}$	*N/A*	Bir Moghrein
Di Biagio et al. (2019)	DB19	*N/A*	*N/A*	*N/A*	19 cases	Across the gl

As natural mineral dust particles can be concave, a direct ε–Ψ_{ens} conversion may induce errors because Ψ_{ens} reflects both macroscopic and small-scale geometric properties of concave particles, while the particle aspect ratio reflects only macroscopic properties. To reduce the influence of small-scale geometric properties in the conversion, we newly define an effective degree of sphericity from Eqs. (1–2) by applying $A_{\mathrm{s}} = 4A_{\mathrm{proj}}$ (Vouk 1948) as

$$\Psi_{\mathrm{eff}} = \frac{\pi^{\frac{1}{3}}(6V)^{\frac{2}{3}}}{4A_{\mathrm{proj}}}, \quad (3)$$

which retains the equivalency to Ψ for a convex particle and to Ψ_{ens} for a convex particle ensemble. By using ε–Ψ_{eff} conversions (see Appendix) with considering various aspect ratio and particle size definitions, we compile the Ψ_{eff} values of the reported mineral dust particles in each particle maximum diameter bin.

Figure 2 shows the size-dependent Ψ_{eff} of mineral dust particles for the 18 cases listed in Table 1. About 62% of size-representative Ψ_{eff} values fall within the prescribed Ψ_{eff} range of the ensemble models. The other cases mainly have been transported for a long-distance and have $\Psi_{\mathrm{eff}} < 0.695$ (Reid et al., 2003a, 2003b; Coz et al., 2009), implying that more irregular or higher aspect ratio particles may dominate. Note that the Ψ_{eff} estimates lower than 0.695 are less precise because they are based on extrapolation of the ε–Ψ_{eff} relationship. Although no distinct size dependence of Ψ_{eff} is found when all cases are integrated, most size-resolved cases with D from 1–10 µm correspond to a slightly larger Ψ_{eff} than the

other size ranges (Kandler et al., 2007; Klaver et al., 2011; Scheuvens et al., 2011; Lieke et al., 2011). Based on these observational constraints, we define three size-dependent particle shape ensemble models: A compact model, moderately irregular model, and severely irregular model (Model 1–3, respectively).

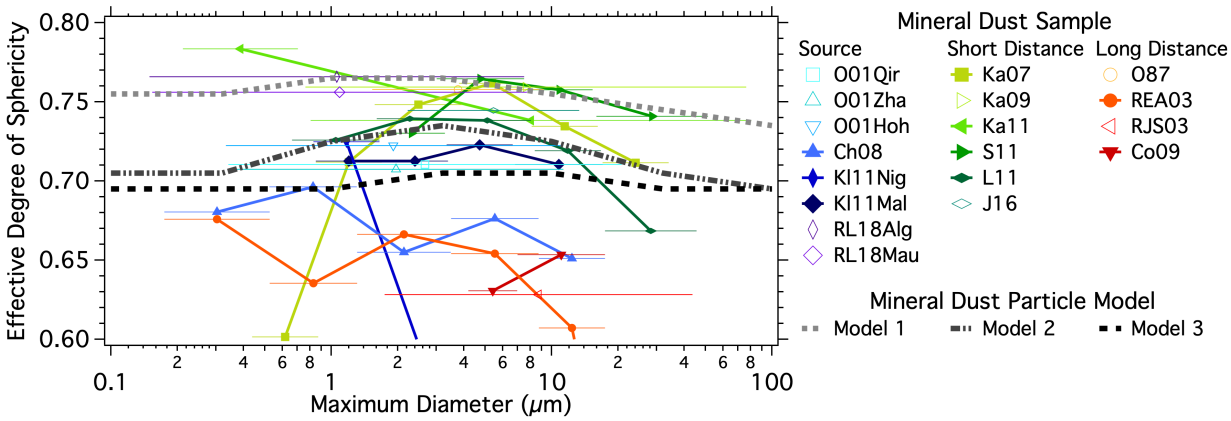

Figure 2. Size-dependent effective degree of sphericity for mineral dust cases in Table 1. Open and closed symbols indicate that mineral dust samples are grouped into single and multiple size bins, respectively. Symbol colors indicate dust samples (blue-purple) collected near the source regions, (green) transported for a short distance, and (red-orange) transported for a long distance, according to Huang et al. (2020). The horizontal bar describes the boundaries of size bins, corrected by $\frac{D}{D_A}$ specified in Fig. 1e. Short-dashed, dash-dot-dotted, and long-dashed lines show size-dependent particle shape ensemble models used in the following analyses.

2.3 Formulation of the bulk backscattering properties

We consider four wavelengths (355, 532, 710, and 1064 nm) at which typical or sophisticated lidar systems can measure backscattering signals (Tesche et al., 2009; Haarig et al., 2018). To take into account a realistic spectral dependence of dust optical properties, we use spectrally resolved CRIs ($\widetilde{m} = m_r - im_i$) of 21 mineral dust aerosol samples collected across the globe (Kandler et al., 2011; Di Biagio et al., 2019). As the Di Biagio et al. spectral range is 370–950 nm, we use the closest available wavelength for the simulations at 355 and 1064 nm.

To simulate the bulk backscattering properties, we integrate the single-scattering properties of mineral dust particles over a particle size distribution (PSD) with D ranging from 0.01–300 µm:

$$n(D) = \frac{1}{\sqrt{2\pi}\ln(\sigma)} \exp\left[-\frac{\ln^2\left(\frac{D}{D_m}\right)}{2\ln^2(\sigma)}\right], \quad (4)$$

where D_m is the median particle diameter. We assume the geometric standard deviation (σ) to be 2.8 (d'Almeida & Schütz, 1983; Goldstein et al., 2005). Based on the PSD and particle shape ensemble models described in Section 2.2,

we obtain the bulk mineral dust backscattering properties, including lidar ratios (S) and depolarization ratios (δ) for various effective radii ($r_{\rm eff}$), at wavelength λ as

$$S_\lambda = \frac{\langle Q_{\rm ext,\lambda}\rangle}{\langle Q_{\rm back,\lambda}\rangle}, \quad (5)$$

$$\delta_\lambda = \frac{\langle P_{11,\lambda}(\pi)\rangle - \langle P_{22,\lambda}(\pi)\rangle}{\langle P_{11,\lambda}(\pi)\rangle + \langle P_{22,\lambda}(\pi)\rangle}, \quad (6)$$

$$r_{\rm eff} = \frac{3\int_{D_{\rm min}}^{D_{\rm max}} n(D)V[D,\Psi_{\rm eff}(D)]d\ln D}{4\int_{D_{\rm min}}^{D_{\rm max}} n(D)A_{\rm proj}[D,\Psi_{\rm eff}(D)]d\ln D}, \quad (7)$$

where the bulk extinction efficiency $\langle Q_{\rm ext}\rangle$, backscattering efficiency $\langle Q_{\rm back}\rangle$, and phase matrix elements in the backscattering direction $\langle P_{\rm ij}(\pi)\rangle$ are described as

$$\langle Q_{\rm ext,\lambda}\rangle = \frac{\int_{D_{\rm min}}^{D_{\rm max}} n(D)A_{\rm proj}[D,\Psi_{\rm eff}(D)]Q_{\rm ext}[D,\widetilde{m}_\lambda,\Psi_{\rm eff}(D)]d\ln D}{\int_{D_{\rm min}}^{D_{\rm max}} n(D)A_{\rm proj}[D,\Psi_{\rm eff}(D)]d\ln D}, \quad (8)$$

$$\langle Q_{\rm back,\lambda}\rangle = \frac{\int_{D_{\rm min}}^{D_{\rm max}} n(D)A_{\rm proj}[D,\Psi_{\rm eff}(D)]Q_{\rm sca}[D,\widetilde{m}_\lambda,\Psi_{\rm eff}(D)]P_{11}[\theta=\pi,D,\widetilde{m}_\lambda,\Psi_{\rm eff}(D)]d\ln D}{4\pi\int_{D_{\rm min}}^{D_{\rm max}} n(D)A_{\rm proj}[D,\Psi_{\rm eff}(D)]Q_{\rm ext}[D,\widetilde{m}_\lambda,\Psi_{\rm eff}(D)]d\ln D}, \quad (9)$$

$$\langle P_{ij,\lambda}(\pi)\rangle = \frac{\int_{D_{\rm min}}^{D_{\rm max}} n(D)A_{\rm proj}[D,\Psi_{\rm eff}(D)]Q_{\rm sca}[D,\widetilde{m}_\lambda,\Psi_{\rm eff}(D)]P_{\rm ij}[\theta=\pi,D,\widetilde{m}_\lambda,\Psi_{\rm eff}(D)]d\ln D}{\int_{D_{\rm min}}^{D_{\rm max}} n(D)A_{\rm proj}[D,\Psi_{\rm eff}(D)]Q_{\rm sca}[D,\widetilde{m}_\lambda,\Psi_{\rm eff}(D)]d\ln D}. \quad (10)$$

The single-scattering properties of the extinction efficiency ($Q_{\rm ext}$), the scattering efficiency ($Q_{\rm sca}$), and the phase matrix elements ($P_{\rm ij}$) are obtained from the TAMUdust2020 database. Furthermore, we analyze a total of 1260 bulk mineral dust optical properties based on combinations of 21 CRIs, three ensemble models, and 20 effective radii ranging from 0.1–10 µm.

3 Backscattering property simulations of various mineral dust aerosols

3.1 Sensitivity to particle size

Figure 3 shows the lidar and depolarization ratios (hereinafter referred to as the S–δ diagram) for various mineral dust particles at wavelength 532 nm. The S–δ diagram exhibits two domains in terms of the single-scattering albedo (SSA): non-absorbing (SSA 0.95) and absorbing. For non-absorbing particles, as $r_{\rm eff}$ increases, S moderately decreases (Fig. 3b), and δ increases (Fig. 3c). For absorbing particles, δ slightly decreases with increased $r_{\rm eff}$. In contrast, S rapidly increases with increased $r_{\rm eff}$ (Fig. 3d) due to the decrease of SSA and $P_{11}(\pi)$, consistent with the field observations (Ryder et al., 2013) that show the strong negative correlation between SSA and $r_{\rm eff}$ of mineral dust particles. As mineral dust particles with low SSA (~0.8) are present according to the field campaigns (Otto et al., 2009; Di Biagio et al., 2019), both particle domains need to be considered to interpret the dust aerosol backscattering properties.

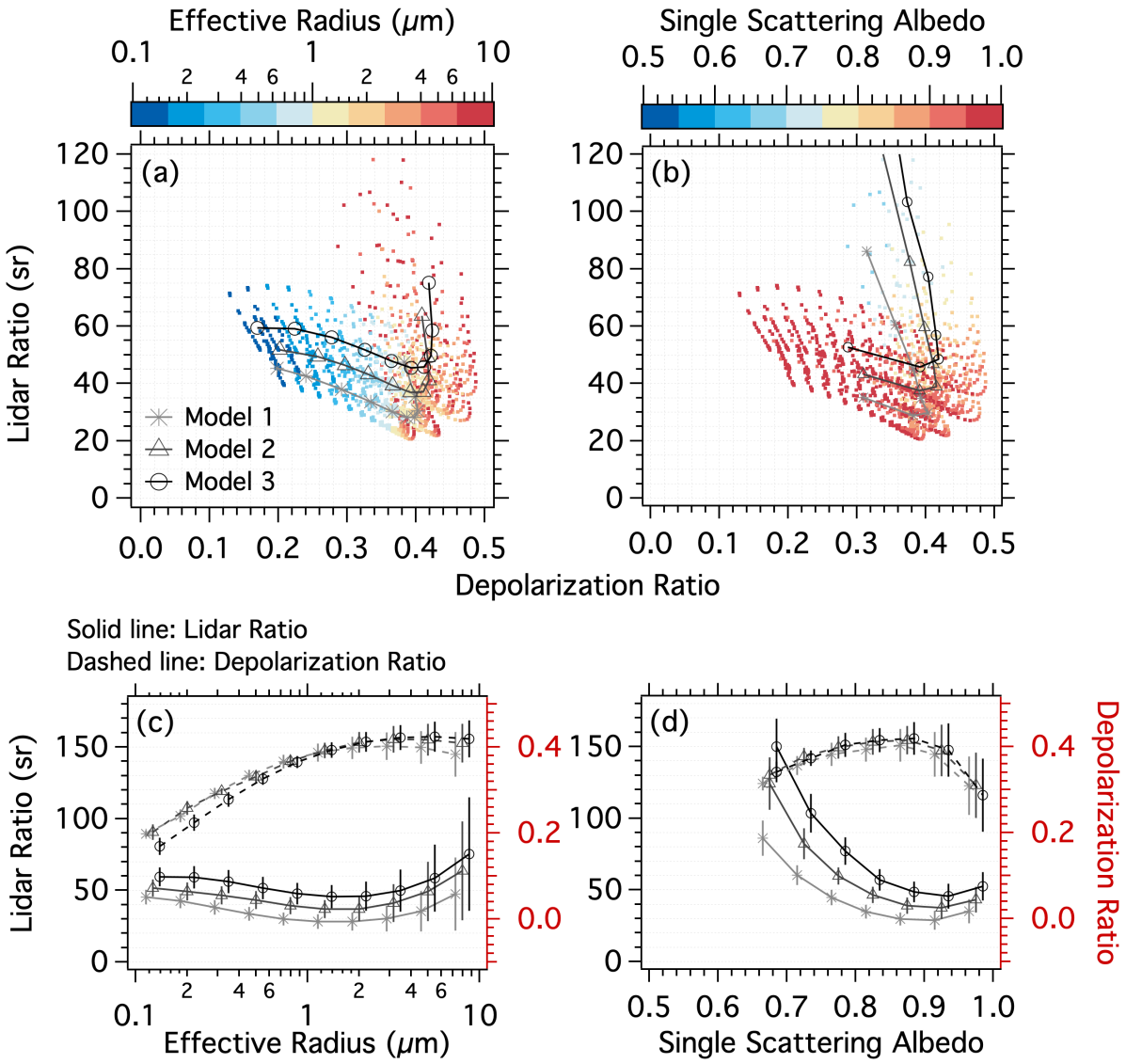

Figure 3. (Upper panels) S–δ diagrams (the lidar ratio and depolarization ratio) at 532 nm for various bulk mineral dust optical property models. Colors indicate (a) the effective radius and (b) the single-scattering albedo of the bulk mineral dust model. (Lower panels) Bin-averaged (solid lines; left axis) lidar ratios and (dashed lines; right axis) depolarization ratios of these mineral dust models are shown as a function of (c) the effective radius and (d) the single-scattering albedo. The vertical bars indicate the standard deviations of these quantities. Bin-averaged S–δ quantities from (c-d) are also plotted as solid lines with symbols in the S–δ diagrams in (a-b).

3.2 Sensitivity to particle shape

The impact of particle shape on S is more significant than that of r_{eff} for non-absorbing particles (Fig. 3c). The difference between the compact and severely irregular models (Models 1 and 3) can be ~20 sr, which is almost as large as that caused by the regional m_{r} difference of mineral dust particles (Schuster et al., 2012; Hofer et al., 2017). This impact is pronounced for absorptive particles (Fig. 3d). These results indicate that knowledge of the particle shape is essential to determine S of mineral dust aerosols, as suggested by earlier studies of small particles (Gasteiger et al., 2011). However, δ shows little sensitivity to particle shape, implying that some important characteristics are omitted from the present model, such as particle roundness (Bi et al., 2018) and small-scale particle surface irregularities (Kahnert et al., 2020). Further investigation to characterize the mineral dust particle shape is necessary. Saito et al. (2021) indicate that degree of sphericity 0.71 achieves excellent consistency in the phase matrix elements of mineral dust particles between laboratory measurements and simulations. Thus, the severely irregular model (i.e., Model 3) is among the best particle shape models.

3.3 Spectral dependence

Figure 4 shows the backscattering properties of the various mineral dust aerosols based on the severely irregular model at wavelengths 355, 532, 710, and 1064 nm. The S–δ diagram shows that non-absorbing particles dominate at longer wavelengths (Fig. 4a–d) due to smaller size parameters and lower m_{i} of particles (Fig. 4f). As a result, backscattering properties of mineral dust aerosols at longer wavelengths tend to be simpler and show monotonic relations with r_{eff}.

The spectral dependence of S varies moderately with r_{eff} due to distinct contributions from CRI in different size domains. S is highly anti-correlated with m_{r} for non-absorbing particles (Schuster et al., 2012), while S is theoretically correlated with m_{i} for larger absorptive ones. Consequently, typical size distributions of mineral dust particles show U-shaped spectral dependences of S (Gasteiger et al., 2011) associated with correlations with CRI (Figs. 4e–g). In addition, the spectral dependence of δ is weak, but the δ values vary with r_{eff} (Fig 4h). Therefore, knowledge of r_{eff} is essential to determine the spectrally dependent backscattering properties of mineral dust plumes.

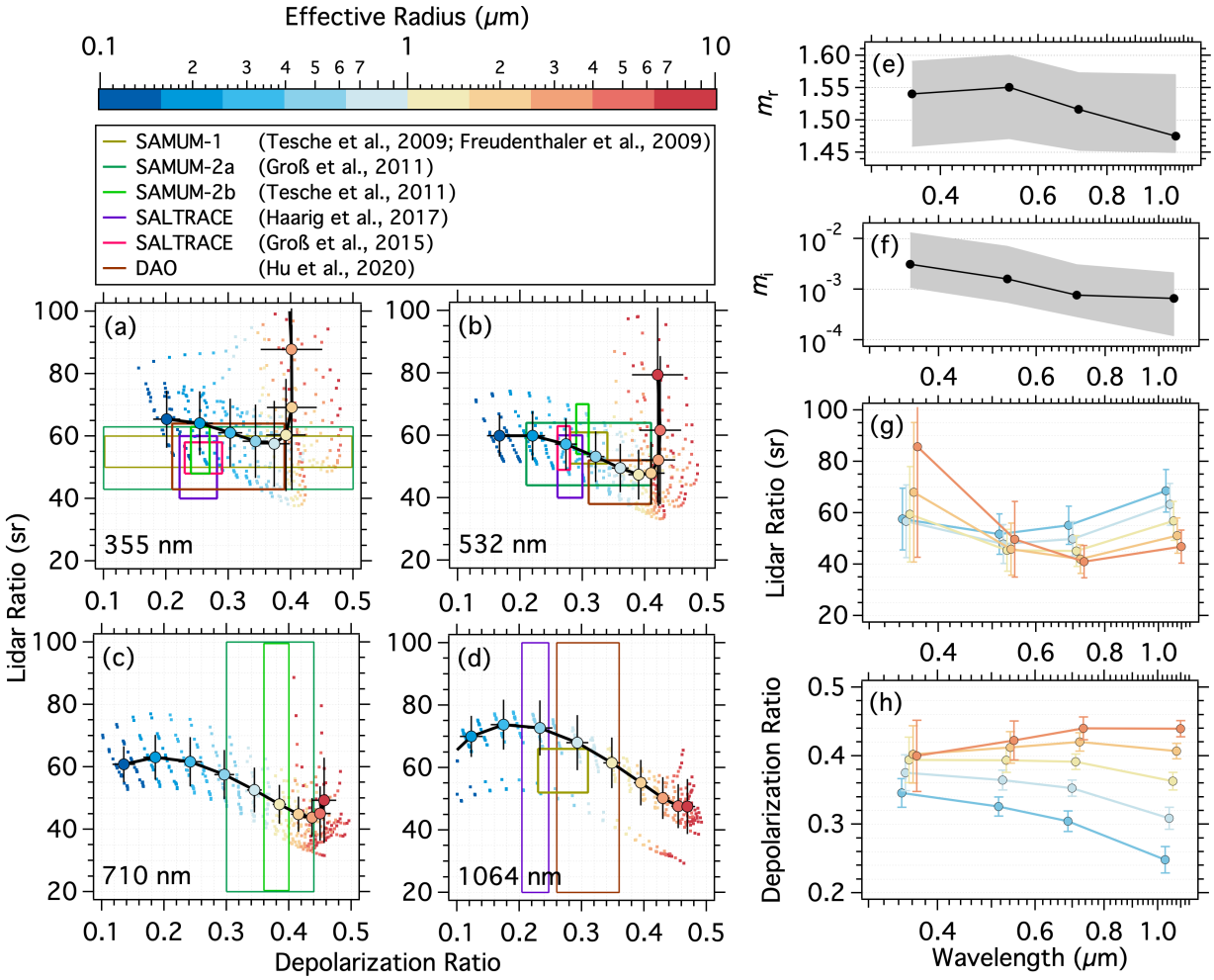

Figure 4. (Left panels a-d) Similar to upper panels in Fig. 3, but for backscattering properties based on Model 3 at four wavelengths including (a) 355 nm, (b) 532 nm, (c) 710 nm, and (d) 1064 nm. Colored rectangles in (a-d) are S–δ ranges for particle samples in field campaigns indicated in the box (Right panels e-h) Median values of (e) the real and (f) imaginary parts of the complex refractive indices (CRI) of various mineral dust particles for the four wavelengths, and the size-bin averaged spectral (g) lidar ratios and (h) depolarization ratios of selected bulk dust optical properties. Gray-shaded ranges and solid lines in panels (e-f) indicate the range and median values of the spectral CRI of 21 mineral dust particle samples. Solid lines and error bars in the panels (a-d, g-h) are bin-averaged backscattering properties and their standard deviations. Color coding in dots and circles in these panels indicates the effective radius.

3.4 Comparison with lidar observations

The simulations of the backscattering properties of mineral dust aerosols are compared to statistics obtained from several field campaigns targeting Saharan (Tesche et al., 2009, 2011; Freudenthaler et al., 2009; Groß et al., 2011, 2015; Haarig et al., 2017) and Asian dust plumes (Hu et al., 2020). Overall, the observed backscattering properties are reasonably consistent with those simulations for r_{eff} ranging from 0.3–1.5 µm, but exhibit slightly lower S at 355 nm (Figs. 4a–d). Moreover, some simulations of mineral dust aerosols with $r_{\text{eff}} > 1.5$ µm show δ beyond the observed range.

The simulations of the depolarization ratio of mineral dust particles at shorter wavelengths such as 355 nm remain a challenge due to large size parameters, leading to more sensitivity to particle shapes and CRI. In addition, a dust plume may include non-dust particles that could noticeably affect the lidar signals. Such factors could lead to an inconsistency in the backscattering properties between observations and simulations at shorter wavelengths.

4 Conclusions and remarks

This study investigates the mineral dust particles' backscattering properties towards elevating the current knowledge of the relationship between the backscattering properties and microphysical properties of mineral dust aerosols. Using an existing single-scattering property database of irregular aerosol particles (TAMUdust2020), we develop robust bulk backscattering property models of mineral dust aerosols. In particular, we constrain the model using reported size-resolved dust particle shape measurements and spectrally resolved dust aerosol CRI measurements made during several field campaigns.

The present results manifest the importance of particle size and shape on the spectral lidar and depolarization ratios. In particular, an appropriate particle shape model is essential to reduce systematic biases in computational lidar ratios. In addition, the effective radius is a crucial factor needed to compute the spectral lidar and depolarization ratios of mineral dust particles. Comparisons with several lidar measurement campaigns confirm the reliability of the bulk dust particle models that achieve spectrally consistent backscattering properties with these measurements.

This study enables the physical interpretation of the backscattering properties of dust plumes to infer microphysical properties of mineral dust aerosols, which has been a challenge for decades. The developed bulk backscattering property models of mineral dust aerosols are applicable to ground-based, aircraft-based, and spaceborne lidar measurements targeting dust plumes (e.g., Ansmann et al., 2003; Winker et al., 2013; Illingworth et al., 2015). In addition, these models are useful for further algorithm development of dust optical property retrievals based on past, current, and future lidar instrument observations.

Acknowledgments and Data Availability

This work was supported by the internal funds (02-132503-00006) and the endowment funds (02-512231-1000) associated with the David Bullock Harris

Chair in Geosciences in the College of Geosciences at Texas A&M University. Ping Yang also acknowledges the support from the National Science Foundation (Grant AGS 1826936). The TAMUdust2020 database is available at Zenodo.org (https://doi.org/10.5281/zenodo.4711247).

Appendix: Polynomial fitting of the degree of sphericity and size ratio

The degree of sphericity (Ψ) and size ratio ($\frac{D}{D_A}$) are fitted in terms of quadratic functions as follows:

$\Psi = a_0 + a_1\varepsilon + a_2\varepsilon^2$, (A1)

$\frac{D}{D_A} = b_0 + b_1\Psi + b_2\Psi^2$, (A2)

where the coefficients are $a_{0,\mathrm{proj}} = 0.75325$, $a_{1,\mathrm{proj}} = 0.16578$, and $a_{2,\mathrm{proj}} = -0.11604$ for $\varepsilon_{\mathrm{proj}}$; $a_{0,\mathrm{el}} = 0.40526$, $a_{1,\mathrm{el}} = 0.60626$, and $a_{2,\mathrm{el}} = -0.22301$ for $\varepsilon_{\mathrm{el}}$; $a_{0,\mathrm{geo}} = 0.8627$, $a_{1,\mathrm{geo}} = 0.035261$, and $a_{2,\mathrm{geo}} = -0.085483$ for $\varepsilon_{\mathrm{geo}}$ in Eq. (A1); and $b_0 = -2.8487$, $b_1 = 15.803$, and $b_2 = -13.224$ in Eq. (A2).

References

Ansmann, A., Bösenberg, J., Chaikovsky, A., Comerón, A., Eckhardt, S., Eixmann, R., et al. (2003). Long-range transport of Saharan dust to northern Europe: The 11–16 October 2001 outbreak observed with EARLINET, *Journal of Geophysical Research Atmosphere*, 108(D24), 4783, doi:10.1029/2003JD003757.

Bangert, M., Nenes, A., Vogel, B., Vogel, H., Barahona, D., Karydis, et al. (2012). Saharan dust event impacts on cloud formation and radiation over Western Europe. *Atmospheric Chemistry and Physics*, 12, 4045–4063. https://doi.org/10.5194/acp-12-4045-2012.

Bi, L., Lin, W., Liu, D., & Zhang, K. (2018). Assessing the depolarization capabilities of nonspherical particles in a super-ellipsoidal shape space. *Optics Express*, 26, 1726–1742. doi:10.1364/oe.26.001726.

Bi, L., Yang, P., Kattawar, G. W., & Kahn, R. (2010). Modeling optical properties of mineral aerosol particles by using nonsymmetric hexahedra. *Applied Optics*, 49, 334–342.

Bi, L., Yang, P., Kattawar, G. W., Hu, Y., & Baum, B. A. (2011). Scattering and absorption of light by ice particles: Solution by a new physical-geometric optics hybrid method. *Journal of Quantitative Spectroscopy and Radiative Transfer,*112, 1492–1508.

Bi, L, Yang, P, Kattawar, G. W., & Mishchenko, M. I. (2013). Efficient implementation of the invariant imbedding T-matrix method and the separation of variables method applied to large nonspherical inhomogeneous particles. *Journal of Quantitative Spectroscopy and Radiative Transfer,* 116, 169–83.

Burton, S., Hair, P., Kahnert, J. W., Ferrare, M., Hostetler, R. A., Cook, C. A., et al. (2015). Observations of the spectral dependence of linear particle depolarization ratio of aerosols using NASA Langley Airborne High Spec-

tral Resolution Lidar, *Atmospheric Chemistry and Physics*, 15, 13453–13473, https://doi.org/10.5194/acp-15-13453-2015.

Chou, C., Formenti, P., Maille, M., Ausset, P., Helas, G., Harrison, M., & Osborne, S. (2008). Size distribution, shape, and composition of mineral dust aerosols collected during the African monsoon multidisciplinary analysis special observation period 0: Dust and biomass-burning experiment field campaign in Niger, January 2006. *Journal of Geophysical Research*, 113, D00C10. https://doi.org/ 10.1029/2008JD009897.

Coz, E., Gómez-Moreno, F. J., Pujadas, M., Casuccio, G. S., Lersch, T. L., & Artíñano, B. (2009). Individual particle characteristics of North African dust under different long-range transport scenarios. *Atmospheric Environment*, *43*(11), 1850–1863. https://doi.org/10.1016/j. atmosenv.2008.12.045

d'Almeida, G. A., & Schütz, L. (1983). Number, mass and volume distributions of mineral aerosol and soils of the Sahara. *Journal of Applied Meteorology and Climatology,* 22, 233–243.

DeMott, P. J., Sassen, K., Poellot, M. R., Baumgardner, D., Rogers, D. C., Brooks, S. D., et al. (2003). African dust aerosols as atmospheric ice nuclei, *Geophysical Research Letters*, 30(14), 1732, doi:10.1029/2003GL017410.

Di Biagio, C., Formenti, P., Balkanski, Y., Caponi, L., Cazaunau, M., Pangui, E., et al. (2019). Complex refractive indices and single-scattering albedo of global dust aerosols in the shortwave spectrum and relationship to size and iron content, *Atmospheric Chemistry and Physics*, 19, 15503–15531.

Di Biagio, C., Balkanski, Y., Albani, S., Boucher, O., & Formenti, P. (2020). Direct radiative effect by mineral dust aerosols constrained by new microphysical and spectral optical data. *Geophysical Research Letters*, 47, e2019GL086186. https://doi.org/ 10.1029/2019GL086186.

Duce, R. A., Unni, C. K., Ray, B. J., Prospero, J. M., & Merrill, J. T. (1980). Long-range atmospheric transport of soil dust from Asia to the tropical North Pacific: temporal variability, *Science*, 209, 1522–1524.

Fernald, F. G. (1984). Analysis of atmospheric lidar observations: Some comments. *Applied Optics,* 23(5), 652–653. https://doi.org/10.1364/ AO.23.000652.

Freudenthaler, V., Esselborn, M., Wiegner, M., Heese, B., Tesche, M., Ansmann, A., et al. (2009). Depolarization ratio profiling at several wavelengths in pure Saharan dust during SAMUM 2006 *Tellus Series B: Chemical and Physical Meteorology,* 61, 165–179, https://doi.org/10.1111/j.1600-0889.2008.00396.x.

Gasteiger, J., Wiegner, M., Groß, S., Freudenthaler, V., Toledano, C., Tesche, M., & Kandler, K. (2011). Modeling lidar-relevant optical properties of complex mineral dust aerosols, *Tellus Series B: Chemical and Physical Meteorology,* 63, 725–741, doi:10.1111/j.1600-0889.2011.00559.x.

Ginoux, P. (2003). Effects of nonsphericity on mineral dust modeling. *Journal of Geophysical Research*, *108*(D2), 4052. https://doi.org/10.1029/2002JD002516.

Goldstein, H., Reynolds, R., Reheis, M., Yount, J., Lamothe, P., & Roberts, H. (2005). Particle size, $CaCO_3$, chemical, magnetic, and age data from surficial deposits in and around Canyonlands National Park, Utah. *Canyonlands Research Bibliography.* Paper 1.

Groß, S., Tesche, M., Freudenthaler, V., Toledano, C., Wiegner, M., Ansmann, A., et al. (2011). Characterization of Saharan dust, marine aerosols and mixtures of biomass-burning aerosols and dust by means of multi-wavelength depolarization and Raman lidar measurements during SAMUM 2, *Tellus Series B: Chemical and Physical Meteorology*, 63, 706–724, https://doi.org/10.1111/j.1600-0889.2011.00556.x.

Groß, S., Freudenthaler, V., Schepanski, K., Toledano, C., Schäfler, A., Ansmann, A., & Weinzierl, B. (2015). Optical properties of long-range transported Saharan dust over Barbados as measured by dual-wavelength depolarization Raman lidar measurements, *Atmospheric Chemistry and Physics*, 15, 11067–11080, https://doi.org/10.5194/acp-15-11067-2015.

Haarig, M., Ansmann, A., Althausen, D., Klepel, A., Groß, S., Freudenthaler, V., et al. (2017) Triple-wavelength depolarization-ratio profiling of Saharan dust over Barbados during SALTRACE in 2013 and 2014, *Atmospheric Chemistry and Physics*, 17, 10767–10794, https://doi.org/10.5194/acp-17-10767-2017.

Haarig, M., Ansmann, A., Baars, H., Jimenez, C., Veselovskii, I., Engelmann, R., & Althausen, D. (2018). Depolarization and lidar ratios at 355, 532, and 1064nm and microphysical properties of aged tropospheric and stratospheric Canadian wildfire smoke, *Atmospheric Chemistry and Physics*, 18, 11847–11861, https://doi.org/10.5194/acp-18-11847-2018.

Hair, J. W., Hostetler, C. A., Cook, A. L., Harper, D. B., Ferrare, R. A., Mack, T. L., et al. (2008). Airborne High Spectral Resolution Lidar for profiling aerosol optical properties, *Applied Optics*, 47, 6734–6752, doi:10.1364/AO.47.006734.

Haywood, J., Francis, P., Osborne, S., Glew, M., Loeb, N., Highwood, E., et al. (2003). Radiative properties and direct radiative effect of Saharan dust measured by the C-130 aircraft during SHADE: 1. Solar spectrum, *Journal of Geophysical Research,* 108(D18), 8577, doi:10.1029/2002JD002687.

Hofer, J., Althausen, D., Abdullaev, S. F., Makhmudov, A. N. Nazarov, B. I., Schettler, G., et al. (2017). Long-term profiling of mineral dust and pollution aerosol with multiwavelength polarization Raman lidar at the Central Asian site of Dushanbe, Tajikistan: Case studies, *Atmospheric Chemistry and Physics*, 17, 14559–14577.

Hu, Q., Wang, H., Goloub, P., Li, Z., Veselovskii, I., Podvin, T., et al. (2020).

The characterization of Taklamakan dust properties using a multi-wavelength Raman polarization lidar in Kashi, China, *Atmospheric Chemistry and Physics*, 20, 13817–13834, https://doi.org/10.5194/acp-20-13817-2020.

Huang, Y., Kok, J. F., Kandler, K., Lindqvist, H., Nousiainen, T., Sakai, et al. (2020). Climate models and remote sensing retrievals neglect substantial desert dust asphericity. *Geophysical Research Letters*, 47, e2019GL086592. https://doi.org/ 10.1029/2019GL086592.

Huang, X., Yang, P., Kattawar, G. W., & Liou, K. N. (2015). Effect of mineral dust aerosol aspect ratio on polarized reflectance. *Journal of Quantitative Spectroscopy and Radiative Transfer,* 151, 97–109.

Illingworth, A. J., Barker, H. W., Beljaars, A., Ceccaldi, M., Chepfer, H., Clerbaux, N., et al. (2015). The EarthCARE satellite: The next step forward in global measurements of clouds, aerosols, precipitation, and radiation, *Bulletin of the American Meteorological Society*, 96, 1311–1332.

Ishimoto, H., Zaizen, Y., Uchiyama, A., Masuda, K., & Mano, Y. (2010). Shape modeling of mineral dust particles for light-scattering calculations using the spatial Poisson-Voronoi tessellation, *Journal of Quantitative Spectroscopy and Radiative Transfer,* 111, 2434–2443, https://doi.org/10.1016/j.jqsrt.2010.06.018.

Jeong, G. Y., Park, M. Y., Kandler, K., Nousiainen, T., & Kemppinen, O. (2016). Mineralogical properties and internal structures of individual fine particles of Saharan dust. *Atmospheric Chemistry and Physics*, *16*(19), 12397–12410. https://doi.org/10.5194/acp-16-12397-2016

Johnson B. R. (1988). Invariant imbedding T-matrix approach to electromagnetic scattering. *Applied Optics,* 27, 4861–4873.

Kahnert, M., Kanngießer, F., Järvinen, E., & Schnaiter, M. (2020). Aerosol-optics model for the backscatter depolarisation ratio of mineral dust particles, *Journal of Quantitative Spectroscopy and Radiative Transfer,* 254, 107177, https://doi.org/10.1016/j.jqsrt.2020.107177.

Kandler, K., Benker, N., Bundke, U., Cuevas, E., Ebert, M., Knippertz, P., et al. (2007). Chemical composition and complex refractive index of Saharan Mineral Dust at Izaña, Tenerife (Spain) derived by electron microscopy. *Atmospheric Environment*, *41*(37), 8058–8074. https://doi.org/10.1016/j.atmosenv.2007.06.047

Kandler, K., Lieke, K., Benker, N., Emmel. C, Küpper, M., Müller-Ebert, D., et al. (2011). Electron microscopy of particles collected at Praia, Cape Verde, during the Saharan Mineral Dust Experiment: Particle chemistry, shape, mixing state and complex refractive index. *Tellus Series B: Chemical and Physical Meteorology*, 63, 475–496, doi:10.1111/j.1600-0889.2011.00550.x.

Kandler, K., Schütz, L., Deutscher, C., Ebert, M., Hofmann, H., Jäckel, S., et al. (2009). Size distribution, mass concentration, chemical and mineralogical composition and derived optical parameters of the boundary layer aerosol at

Tinfou, Morocco, during SAMUM 2006. *Tellus Series B: Chemical and Physical Meteorology*, *61*(1), 32–50. https://doi.org/10.1111/j.1600-0889.2008.00385.x

Klaver, A., Formenti, P., Caquineau, S., Chevaillier, S., Ausset, P., Calzolai, G., et al. (2011). Physico-chemical and optical properties of Sahelian and Saharan mineral dust: In situ measurements during the GERBILS campaign. *Quarterly Journal of the Royal Meteorological Society*, *137*(658), 1193–1210. https://doi.org/10.1002/qj.889

Klett, J. D. (1985). Lidar inversion with variable backscatter/extinction ratios. *Applied Optics*, 24(11), 1638–1643. https://doi.org/10.1364/AO.24.001638

Kok, J. F., Ridley, D. A., Zhou, Q., Miller, R. L., Zhao, C., Heald, C. L., et al. (2017). Smaller desert dust cooling effect estimated from analysis of dust size and abundance. *Nature Geoscience,* 10, 274–278.

Lieke, K., Kandler, K., Scheuvens, D., Emmel, C., Glahn, C. V., Petzold, A., et al. (2011). Particle chemical properties in the vertical column based on aircraft observations in the vicinity of Cape Verde Islands. *Tellus Series B: Chemical and Physical Meteorology*, *63*(4), 497–511. https://doi.org/10.1111/j.1600-0889.2011.00553.x

Lindqvist, H., Jokinen, O., Kandler, K., Scheuvens, D., & Nousiainen, T. (2014). Single scattering by realistic, inhomogeneous mineral dust particles with stereogrammetric shapes, *Atmospheric Chemistry and Physics*, 14, 143–157, https://doi.org/10.5194/acp-14-143-2014.

Mishchenko, M. I., Travis, L. D., Kahn, R. A., & West, R. A. (1997). Modeling phase functions for dustlike tropospheric aerosols using a shape mixture of randomly oriented polydisperse spheroids. *Journal of Geophysical Research*, 102(D14), 16831–16847. https://doi.org/10.1029/ 96JD02110.

Okada, K., Heintzenberg, J., Kai, K., & Qin, Y. (2001). Shape of atmospheric mineral particles collected in three Chinese arid-regions. *Geophysical Research Letters*, *28*(16), 3123–3126. https://doi.org/10.1029/2000GL012798.

Okada, K., Kobayashi, A., Iwasaka, Y., Naruse, H., Tanaka, T., & Nemoto, O. (1987). Features of individual Asian dust-storm particles collected at Nagoya, Japan. *Journal of the Meteorological Society of Japan*, *65*(3), 515–521. https://doi.org/10.2151/ jmsj1965.65.3_515

Otto, S., Bierwirth, E., Weinzierl, B., Kandler, K., Esselborn, M., Tesche, M., et al. (2009). Solar radiative effects of a Saharan dust plume observed during SAMUM assuming spheroidal model particles, *Tellus Series B: Chemical and Physical Meteorology*, 61, 270– 296, doi:10.1111/j.1600-0889.2008.00389.x.

Prospero, J. M., & T. N. Carlson (1972), Vertical and areal distribution of Saharan dust over the western equatorial north Atlantic Ocean, *Journal of Geophysical Research*, 77(27), 5255–5265, doi:10.1029/JC077i027p05255.

Reid, E. A., Reid, J. S., Meier, M. M., Dunlap, M. R., Cliff, S. S., Broumas,

A., et al. (2003a). Characterization of African dust transported to Puerto Rico by individual particle and size segregated bulk analysis. *Journal of Geophysical Research,* 108(D19), 8591. https://doi.org/10.1029/ 2002JD002935.

Reid, J. S., Jonsson, H. H., Maring, H. B., Smirnov, A., Savoie, D. L., Cliff, S. S., et al. (2003b). Comparison of size and morphological measurements of coarse mode dust particles from Africa. *Journal of Geophysical Research*, *108*(D19), 8593. https://doi.org/10.1029/ 2002JD002485

Rocha-Lima, A., Martins, J. V., Remer, L. A., Todd, M., Marsham, J. H., Engelstaedter, S., et al. (2018). A detailed characterization of the Saharan dust collected during the Fennec campaign in 2011: In situ ground-based and laboratory measurements. *Atmospheric Chemistry and Physics*, *18*(2), 1023–1043. https://doi.org/10.5194/acp-18-1023-2018

Ryder, C. L., Highwood, E. J., Rosenberg, P. D., Trembath, J., Brooke, J. K., Bart, M., et al. (2013). Optical properties of Saharan dust aerosol and contribution from the coarse mode as measured during the Fennec 2011 aircraft campaign, *Atmospheric Chemistry and Physics*, 13, 303–325.

Saito, M., Yang, P., Ding, J., & Liu, X. (2021) A comprehensive database of the optical properties of irregular aerosol particles for radiative transfer simulations. *Journal of the Atmospheric Sciences*, in press, https://doi.org/10.1175/JAS-D-20-0338.1

Scheuvens, D., Kandler, K., Küpper, M., Lieke, K., Zorn, S. R., Ebert, M., et al. (2011). Individual-particle analysis of airborne dust samples collected over Morocco in 2006 during SAMUM 1. *Tellus Series B: Chemical and Physical Meteorology*, *63*(4), 512–530. https://doi.org/10.1111/j.1600-0889.2011.00554.x

Schuster, G. L., Vaughan, M., MacDonnell, D., Su, W., Winker, D., Dubovik, O., et al. (2012). Comparison of CALIPSO aerosol optical depth retrievals to AERONET measurements, and a climatology for the lidar ratio of dust, *Atmospheric Chemistry and Physics*, 12, 7431–7452, doi:10.5194/acp-12-7431-2012.

Sokolik, I. N., & Toon, O. B. (1999). Incorporation of mineralogical composition into models of the radiative properties of mineral aerosol from UV to IR wavelengths, *Journal of Geophysical Research Atmosphere*, 104(D8), 9423–9444, doi:10.1029/1998JD200048.

Sugimoto, N., Matsui, I., Shimizu, A., & Nishizawa, T. (2008). Lidar Network for Monitoring Asian Dust and Air Pollution Aerosols, *IEEE International Geoscience and Remote Sensing Symposium, 2008, 2,* 573–576, https://doi.org/10.1109/IGARSS.2008.4779057.

Sun, B., Yang, P., Kattawar, G. W., & Zhang, X. (2017). Physical-geometric optics method for large size faceted particles. *Optics Express,* 25, 24044–24060.

Tesche, M. Ansmann, A. Müller, D., Althausen, D., Mattis, I., Heese, B., et al. (2009). Vertical profiling of Saharan dust with Raman lidars and airborne

HSRL in southern Morocco during SAMUM, *Tellus Series B: Chemical and Physical Meteorology*, 61(1), 144-164, DOI: 10.1111/j.1600-0889.2008.00390.x

Ulanowski, Z., Bailey, J., Lucas, P. W., Hough, J. H., & Hirst, E. (2007). Alignment of atmospheric mineral dust due to electric field. *Atmospheric Chemistry and Physics*, *7*(24), 6161–6173. https://doi.org/10.5194/acp-7-6161-2007

Van der Does, M., Knippertz, P., Zschenderlein, P., Giles Harrison, R., & Stuut, J.-B. W. (2018). The mysterious long-range transport of giant mineral dust particles. *Science Advances*, *4*(12), eaau2768. https://doi.org/10.1126/sciadv.aau2768

Vouk, V. (1948). Projected area of convex bodies. *Nature,* 162, 330-331.

Wadell, H. (1935). Volume, shape and roundness of quartz particles. *Journal of Geology,* 43, 250–280.

Winker, D. M., Tackett, J. L., Getzewich, B. J., Liu, Z., Vaughan, M. A., & Rogers, R. R. (2013). The global 3-D distribution of tropospheric aerosols as characterized by CALIOP, *Atmospheric Chemistry and Physics*, 13, 3345–3361, https://doi.org/10.5194/acp-13-3345-2013.

Yang, P., Ding, J., Panetta, R. L., Liou, K.-N., Kattawar, G. W., & Mishchenko, M. I. (2019). On the convergence of numerical computations for both exact and approximate solutions for electromagnetic scattering by nonspherical dielectric particles, *Progress in Electromagnetic Research*, 164, 27–61.

Yang, P., & Liou, K. N. (1996). Geometric-optics-integral-equation method for light scattering by nonspherical ice crystals, *Applied Optics*, 35, 6568–6584.

Yang, P., & Liou, K. N. (1997). Light scattering by hexagonal ice crystals: Solution by a ray-by-ray integration algorithm, *Journal of the Optical Society of America A.*, 14, 2278-2289.

Yorks, J. E., McGill, M. J., Palm, S. P., Hlavka, D. L., Selmer, P. A., Nowottnick, E. P., et al. (2016). An overview of the CATS level 1 processing algorithms and data products, *Geophysical Research Letters*, 43, 4632–4639, doi:10.1002/2016GL068006.